Application of a Parallel DSMC Technique to Predict Flow Characteristics in Microfluidic Filters

Ozgur Aktas, N. R. Aluru, *Member, IEEE*, and Umberto Ravaioli, *Senior Member, IEEE*

***Abstract*—Using a parallel implementation of the direct simulation Monte Carlo (DSMC) method, periodic MEMS microfilters are studied in detail. The dependence of the flow characteristics on geometry, Knudsen number, pressure difference, spacing between the filter elements, and accommodation coefficients are investigated. By comparing DSMC results with the widely used analytical formulas, the validity range of the analytical approaches is evaluated. The simulation results show that velocity slip exists both on the filter channel walls and on the filter membrane and results in an increased flow rate. Velocity slip increases strongly with decreasing accommodation coefficients. For long channels, this results in a strong increase in flow rate; whereas for short channels, the increase in flow rate is limited. For the filter separations considered in this paper, we observe that separation between filter channels does not influence the flow rate within each channel. [636]**

***Index Terms*—Incomplete accommodation, microfilters, microfluidics, parallel direct simulation Monte Carlo (DSMC), rarefied gas dynamics, slip flow.**

I. Introduction

RECENT advances in MEMS technology have enabled the fabrication of a number of microfluidic applications [1]–[5]. In many of these MEMS applications, the operation and performance of the microdevice depends directly or indirectly on gas dynamics. The role of the gas flow on the performance of microbearings, oscillating thin films, comb drives, hard-drive heads, and microthrusters has been investigated before [6]–[9]. This paper reports on gas flow through microfilters.

Microfluidic filters have been demonstrated and investigated experimentally [4]. The filters were fabricated by opening holes of about 5 μm radius on a 1-μm-thick silicon membrane. The membranes were coated with a polymer layer to obtain a burst pressure of about 0.25 atm. The opening ratio (defined as the ratio of the open area of the filter to the total area) of these filters was about 20%. Some work has also been reported on filter-like structures with 100-nm openings for liquid- and gas-based applications [5]. Even though these filters had a smaller opening ratio, they were tested for a much larger pressure difference of 1.17 atm.

The experimental studies on microfilters are of great importance as they demonstrate that filters can be made sufficiently thin and strong to provide useful flow rates. Higher flow rates are always desirable, as they allow for filtering of larger volumes in a given time. The flow rate of a filter can be increased by using a larger pressure difference, a larger opening ratio, or a thinner filter membrane. However, there are a number of tradeoffs involved. For example, the maximum pressure difference that can be applied is limited by the burst pressure of the filter. The burst pressure can be increased by increasing the membrane thickness or by reducing the opening ratio—both of which result in a lower flow rate. The pressure difference may also be limited by power-consumption requirements and by the capabilities of MEMS pumps. These limitations necessitate the optimization of filter parameters for obtaining the maximum flow rate.

The small dimensions encountered in microfilters imply that the flow is rarefied in these devices. The amount of rarefaction is quantified through Knudsen number (Kn), which is defined as the ratio of the mean free path of gas molecules to a characteristic length. As the device dimensions get smaller, the Kn and the rarefaction effects will increase. Due to the limits on pressure, the flow velocity is subsonic in microfilters, i.e., high Mach numbers (M) are not achieved. Thus, the microfilters generally operate in a high-Knudsen/low-M regime. As the characteristic device dimensions shrink, the high-Kn/low-M flow regime becomes increasingly common. Thus, the methods developed for studying microfilters can be applied to a large number of microfluidic flows.

The direct simulation Monte Carlo (DSMC) method is widely employed for simulation of flows with $0.1 < Kn$ [12], [13]. This technique was previously used for investigation of gas flow in MEMS devices [10], [11]. However, much of the previous work was limited to transonic and supersonic flows and simple two-dimensional (2-D) channel structures. For microfilters, the flow velocity is much lower and the filter channels have a smaller length-to-height ratio. In many cases, the flow can no longer be assumed to be fully developed. To model these effects, in this paper, complete devices with small pressure differences are considered. This increases the computational load and necessitates the use of parallel computers. We have developed a parallel implementation of the DSMC method (referred to as μMC in the rest of this paper) to simulate microfilters in realistic times.

A. Why Is DSMC Needed for Microflow Simulation?

Gas flow needs to be simulated using different physical models depending on the Kn. The classification of the flow regimes and the need for using appropriate models in each flow regime is well known [7], [10], [18] and is summarized in Table I. Boltzmann's equation is valid in all Kn regimes, but for $Kn < 0.1$, microscale gas flows can be modeled

Manuscript received October 25, 2000; revised June 1, 2001. This work was supported by the Defense Advanced Research Projects Agency. The work of N. R. Aluru was supported by the National Science Foundation under an NSF CAREER Award. The work of O. Aktas was supported by CSE under a Fellowship. Subject Editor S. D. Senturia.

The authors are with the Beckman Institute for Advanced Science and Technology, University of Illinois at Urbana-Champaign, Urbana, IL 61801 USA.

Publisher Item Identifier S 1057-7157(01)08269-5.

TABLE I
PHYSICAL MODELS SUITABLE FOR GIVEN Kn RANGES

$0 < Kn < 0.01$	Continuum flow	Navier-Stokes equation
$0.01 < Kn < 0.1$	Slip flow	Navier-Stokes + slip BC
$0.1 < Kn < 10$	Transition regime	Boltzmann equation
$10 < Kn$	Free flow	Collisionless Boltzmann eqn.

more conveniently by the Navier–Stokes equations. For $0.01 < Kn < 0.10$, Navier–Stokes equations need to be used with first-order slip boundary conditions. For $Kn > 0.10$, it is necessary either to use equations that represent the higher order moments of the Boltzmann equation, such as the Burnett equations, or to solve the Boltzmann equation itself. Burnett equations are applicable in the lower Kn range of the transition regime. Solution of the linearized Boltzmann equation has also been studied in detail. However, both of these methods present difficulties for application to general geometries.

Considerable work on slip boundary conditions has appeared in the literature. Various second-order slip boundary conditions for use with the Burnett equations have been presented and compared [7]. The lack of agreement on the coefficients in the expression for the second-order slip boundary conditions presents difficulties. In [7], it was demonstrated that all models have errors in predicting the normalized velocity profile, and that a tradeoff between the accuracy of the flow rate and the normalized velocity profile exists. In an alternative approach [7], a higher order boundary condition and a scaling law for viscosity for use with the Burnett equations were proposed. Using this model, it was shown that both the velocity profile and the flow rate can be reproduced for channel, pipe, and duct flows. However, the applicability of this approach is limited, as it employs variables that are in general used as fitting parameters.

The DSMC technique is applicable in all Kn regimes and has been shown to simulate an equation close to the Boltzmann equation [14]. It can capture all of the rarefaction effects correctly without using any fitting parameters. In addition, it is relatively easy to include additional physics, such as surface reactions and ionization. Although DSMC is computationally intensive, it can be efficiently parallelized, and practical turn-around times can be achieved. The issues encountered in applying DSMC to microflows are further discussed at the end of Section II.

II. SPECIFICS OF THE DSMC IMPLEMENTATION

DSMC is a statistical and particle-based method in which a number of representative particles are followed in space and time. Each simulated particle represents w_p real particles, where w_p is the particle weight. The time evolution of particle positions and velocities are simulated separately. Time is divided into small steps of Δt, which needs to be smaller than the average time between collisions in order to obtain accurate results. During each time step, the simulated particles undergo free flight without interacting with other particles. If during the free flight a simulated particle hits a surface, its velocity is updated as dictated by the surface model employed. At the end of the time step, the simulated particles undergo collisions according to a statistically accurate collision model. To implement the particle–particle collisions, the simulation domain is divided into a number of cells, and the collision partners are selected according to a collision model from the particles that are in the same cell.

The mean flow properties are obtained as local averages of the individual particle properties. For example, in this work, the mean properties of the flow were estimated for each collision cell. The number of samples that needs to be taken depends on the noise level desired. As with any statistical method, noise is inversely proportional to the square root of the number of samples. The applications considered in this paper require a large number of samples, since the mean velocity is typically much smaller compared to the thermal velocity of the particles. For this reason, it is important to specify the maximum noise level that will allow the desired accuracy. In this work, the maximum noise level on the velocity estimates is about 1.0 m/s. However, it is clear that for cases where a much smaller noise level is desired, the number of samples can become prohibitive.

Our implementation of DSMC follows the fundamental principles outlined in [12]. Specifically, the no-time-counter algorithm has been used to select collision partners. The variable-hard-spheres (VHS) model was used for calculating the collision cross-sections and the final velocities. Internal degrees of freedom of the molecules were ignored. The applicability of the VHS model and the validity of ignoring the internal degrees of freedom were checked by comparing the results with simulations that use a variable-soft-spheres model with the internal degrees of freedom. A constant time step and a constant particle weight were used for all the simulations. A particle cloning technique was employed to decrease the computational time required to simulate the transient [15].

Collision of particles with surfaces can be modeled by using several models. The simplest model assumes diffusive scattering. However, this model fails under a number of conditions. For example:

1) when the surface under study is smooth, i.e., the surface root mean square roughness is small and thoroughly outgassed;
2) when the gas molecules are much lighter compared to the surface molecules;
3) when the translational energy of the gas molecules with respect to the surface is large [12].

The first two cases provide an interesting opportunity for MEMS devices, since MEMS fabrication processes can yield smooth and clean surfaces. Under the listed conditions, the state of the reflected particle depends on the state of the incoming particle, in which case the surface is said to have incomplete accommodation. The Cercignani–Lampis model has been used to capture the effects of incomplete accommodation [16], [17]. In this model, tangential and normal energy accommodation coefficients are used to model the interaction of a given surface–gas pair. The accommodation coefficients summarize the details of interaction of gas molecules with a given surface and

depend on the details of preparation of the surface. Thus, these parameters cannot be estimated easily and shall be treated as parameters that will be obtained experimentally.

The microfluidic geometry is defined as a collection of volumes enclosed by analytical surfaces that are defined in computational boxes. Complex device geometries are represented as a combination of these volumes. For implementing the collisions, uniform Cartesian cells were defined within the computational boxes. Thus the representation of cells and surfaces is independent. Although not used in this work, partial cells are accounted for by calculating the volume of the part remaining in the simulation domain. This approach to the definition of the cells and the simulation domain enables efficient checking of particle–surface interactions without having to trace the particles from cell to cell. Cartesian cells are an efficient method for implementing collisions and allow for efficient parallelization.

To enforce boundary conditions at the input and the output, the simulation domain is interfaced with a gas stream that extends outside of the simulation domain. Boundaries with a stream outside the simulation domain are implemented by injecting particles from the interface into the simulation domain and removing any particles that leave the simulation domain. The injected particles are sampled from a displaced Maxwellian distribution with the local pressure, temperature, and velocity of the interface. To simulate a low-velocity pressure-driven flow, the boundary pressure and temperature were fixed and the local mean velocity was updated by extrapolation of the estimates that develop close to the interface. The effect of fixed temperature was verified to be negligible via a comparison with a simulation for which the temperature was updated self-consistently in the same manner.

DSMC has been used extensively in simulation of rarefied flows. However, for its application to flows in MEMS devices, several difficulties exist. The first one is due to computational cost associated with the large number of samples required for low-velocity flows. This can be alleviated, to a certain extent, by using efficient techniques in implementing DSMC together with parallelization. In addition, statistical properties of the method can be utilized to extract information about the behavior of a given system from seemingly noisy data. However, in general, this issue presents a limitation for the applicability of DSMC to very low-speed flows. The second difficulty in applying DSMC to microfluidics is the requirement of accommodation coefficients. Even though tabulations of experimental accommodation coefficients are available for some materials, the need for experimental data limits the predictive capability of DSMC.

III. Parallel Implementation of DSMC Method

Parallel supercomputers are required for realistic device simulations using DSMC. The design of a parallel program is influenced strongly by the target architecture. In this work, a parallel implementation of the DSMC method is developed for distributed memory parallel computers. In such architectures, a large number of processors (CPUs) are connected with communication hardware of varying complexity and speed. Message passing is a common communication paradigm that can be realized on both distributed and shared memory computers. Standard message-passing interfaces and libraries ensure portability of the code across various platforms. μMC uses the message passing interface and associated libraries for communication between the processors.

Domain decomposition methods were used previously for parallelization of the DSMC algorithm [19], [20]. The DSMC method is suitable for parallelization by domain decomposition, as all the information necessary for particle movement and collisions is localized to cells. During the implementation of a time step in each cell, only the information about particles in that cell, maximum collision probability, and the average number of particles in that cell are required. The interaction of particles with surfaces can also be checked by using local information.

The key issues in the parallel implementation, namely, the domain decomposition and the communication steps, are discussed below in more detail, and the approach taken in μMC is explained.

A. Domain Decomposition

In the domain decomposition step, the simulation domain is broken into several subdomains, and each subdomain is assigned to a separate processor. In the μMC program, the decomposition is performed by dividing the boxes used for the definition of the geometry into slices along a decomposition axis, which is specified by the user for each box. This method is illustrated in Fig. 1(d) and (e). The size of these slices is determined such that load balancing will be achieved when these slices are assigned to processors. For determining the size of each slice, computational load per unit length is measured in each box as a function of position on the decomposition axis. In μMC, an estimate of particle density per unit length is used as the load measure. This simple load measure was observed to give satisfactory results.

B. Communication

Most of the communication required in a parallel implementation of DSMC with domain decomposition is to account for particles that change CPUs. The information of such particles has to be exchanged between CPUs at every iteration. The communication scheme resulting from a sample decomposition is shown in Fig. 1(f). The links denote CPUs that exchange messages at every iteration. Two CPUs exchanging particles will be called neighbors. In μMC, each CPU sends to each of its neighbors one data packet containing the position, velocity, and type of the outgoing particles.

Typically, additional communication is necessary for adapting the cell sizes and particle weight to local properties. If a cell refinement on a particular CPU reduces the number of particles per cell below the acceptable limit, other CPUs must be informed that a particle cloning is required. For this reason, a global communication operation is performed after each period of mean free path estimation. Also, prior to domain decomposition, the estimates for load per unit length are passed on to each CPU by a global communication operation.

The communication overhead can be avoided to a certain degree if communication is overlapped with computation. The approach taken in μMC is depicted in Fig. 2. The program initializes the communication step after the final positions of the

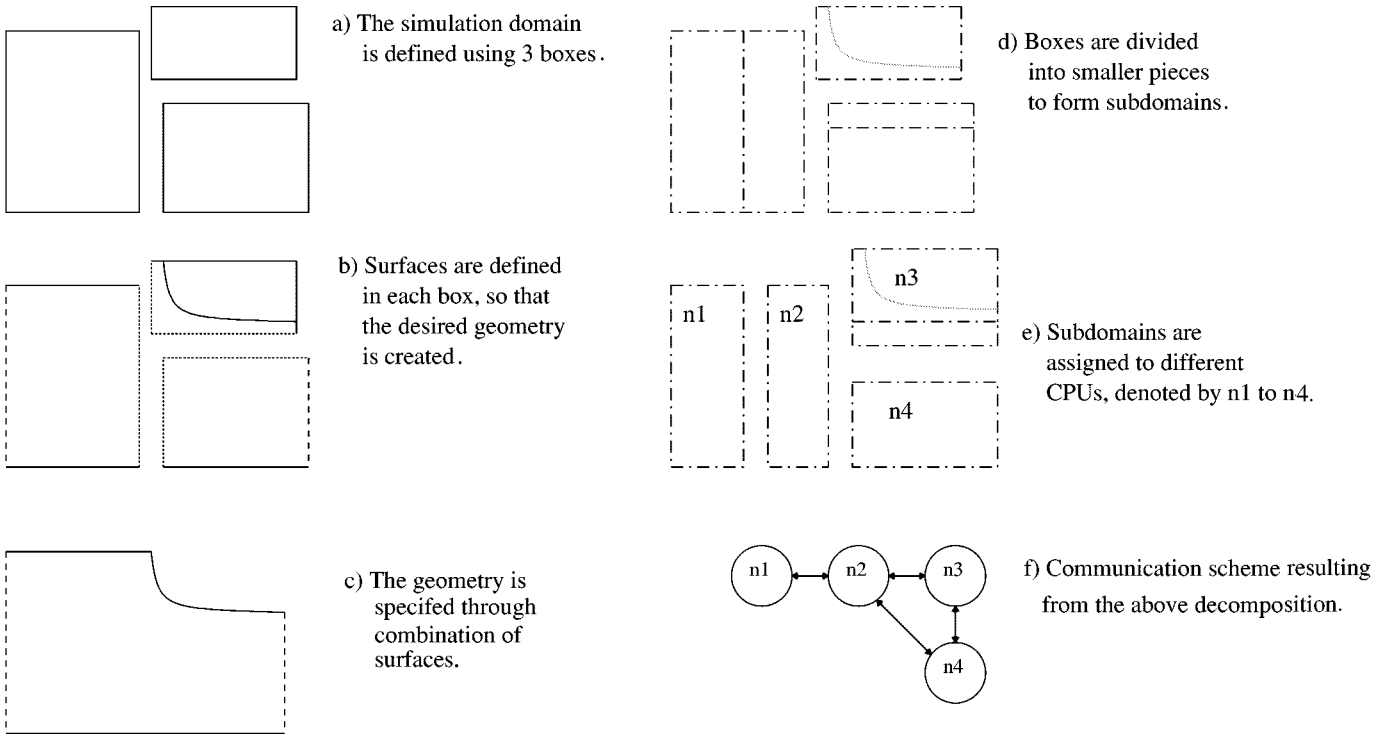

Fig. 1. A sample geometry representation, domain decomposition, and resulting communication scheme is shown. Continuous, dotted, and dashed lines denote reflective, transparent, and boundary surfaces, respectively. Dot-dashed surfaces are used to denote boundaries of subboxes.

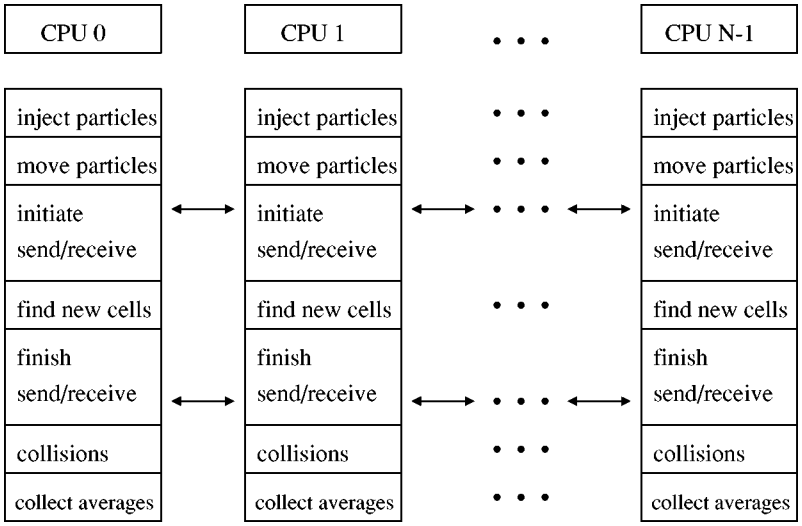

Fig. 2. Sketch showing the placement of communication steps within the DSMC algorithm.

particles are calculated, and communication is overlapped with the calculations necessary to determine the cells of the particles. Next, the messages are received and the cells of the incoming particles are determined.

C. Scaling Characteristics

The parallel performance of μMC was tested using a two-dimensional channel simulation. Two tests, with different loading conditions, were made. In the first test (defined as the scaled load case), the problem size was increased proportionally to the number of CPUs. That is, the length of the channel simulated on each CPU was kept constant, and the total channel length was increased accordingly. In the second test (defined as the constant load case), the problem size was kept fixed and the number of CPUs was changed. In this case, the length of the channel assigned to each CPU decreases with an increasing number of CPUs. The tests were made on the NT-Supercluster of NCSA.

For the scaled load case, the speedup is defined as $N * Ts_1/Tp_N$, where N is the number of CPUs, Ts_1 is the simulation time of the serial code using channel length l, and Tp_N is the parallel simulation time with N CPUs using a channel of length $N * l$. For the constant load case, the speedup was defined as Ts/Tp, where Tp and Ts are the parallel and serial simulation times, respectively.

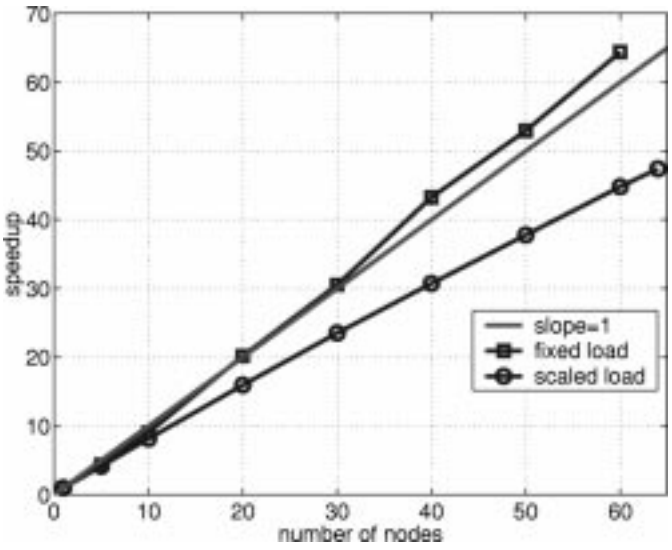

Fig. 3. Scaling characteristics of μMC compared with the linear curve of slope 1.

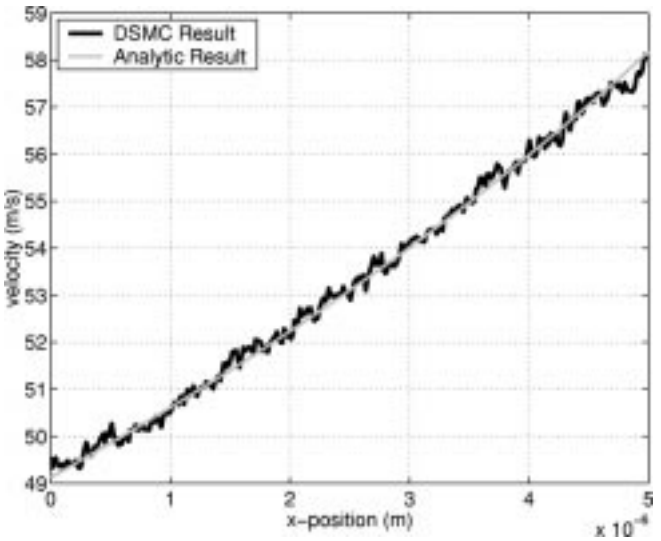

Fig. 4. Comparison of DSMC and analytical results for streamwise velocity along midline.

The measured scaling characteristic is shown in Fig. 3. When the problem size is increased with the number of CPUs, the scaling characteristics exhibit a linear curve for up to 64 CPUs. In this range, no sign of saturation in speedup is observed; however, the slope is less than one, indicating the presence of overhead from parallelization. For the fixed load case, the speedup curve goes above the linear line with slope 1, which can be attributed to the fact that total memory bandwidth increases with the increase in the number of CPUs.

These results demonstrate that the μMC implementation achieves good scaling on distributed memory architectures. All of the simulations reported in this paper were run on parallel machines utilizing up to 64 CPUs.

IV. Code Validation

The μMC code was validated by comparing DSMC results with analytical solutions for rarefied channel flow. Analytical solutions for the rarefied channel problem using first-order slip boundary conditions were given earlier by Arkilic *et al.* [8]. These results were verified to match with DSMC solutions when $Kn < 0.16$ [10].

For purposes of comparison, a pressure-driven flow in a 1-μm-high and 5-μm-long channel was simulated at conditions such that the Kn at the output was 0.03 and the input-to-output pressure ratio was 1.193. Under these conditions, DSMC results are expected to match the first-order slip solution. The plots for velocity and pressure along the midline of the channel are shown together with the analytical solution in Figs. 4 and 5. The simulation was run on a parallel machine with 32 CPUs. Good agreement is observed, thus validating the μMC implementation.

In addition to the channel test, the viscosity of the working gas at 300 K was estimated from a simulation of Couette flow, as described in [12]. Several runs were made using different particle weights, each resulting in a slightly different cell size. The estimates of viscosity varied by $\pm 2\%$ around the expected value.

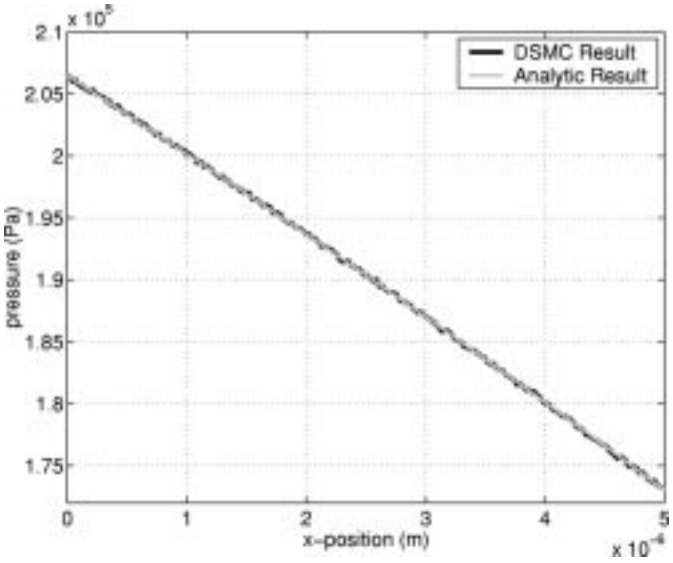

Fig. 5. Comparison of DSMC and analytical results for pressure.

V. Simulation of Microfilter Elements

The flow characteristics in microfilters under rarefied flow conditions are studied in this section. The filter element studied is shown in Fig. 6. The surfaces shown with bold lines, G and J, correspond to the physical filter surfaces, where fully accommodating diffusive reflection boundary conditions are applied, unless specifically mentioned otherwise. The length and height of the filter channel are denoted by l_c and h_c, respectively. The geometry includes an input region of length l_{in} and an output region of length l_{out}. Periodic boundary conditions are applied on surfaces C, D, E, and F to properly simulate a periodic array of filter elements. Fixed pressure boundary conditions are applied along surfaces A and B as described in Section II. The temperature of the input and output streams was kept at 300 K. In all cases, the pressure at the output (B) was held at atmospheric pressure, and the input pressure was varied for changing the pressure difference. A pressure difference of 0.3 atm was used

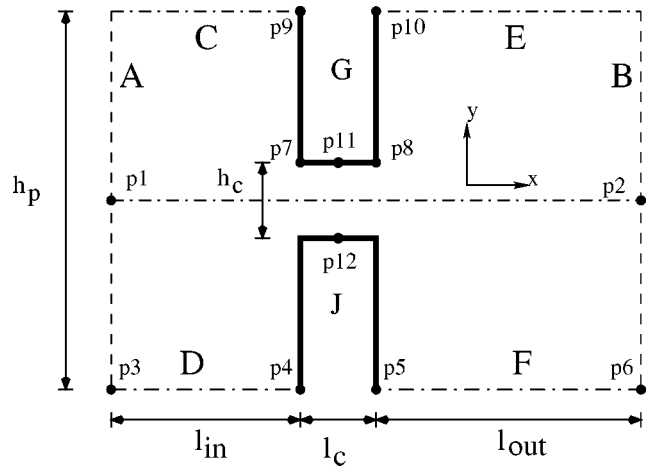

Fig. 6. Description of the filter geometry studied in this work.

in all the simulations, except for the ones that were performed for investigation of dependence of flow rate on the pressure difference.

A time step of 10 ps was used in all the simulations. Particle weight was chosen to satisfy the requirements on minimum particles per cell. Three cloning operations were performed at 0.8, 1.2, and 1.4 μs. Another 0.4 μs was simulated before the averaging was started. The averages were collected for at least 0.6 μs. To reduce noise, for cases with low velocity, this was increased to 1.7 μs. Nitrogen was used as the working fluid.

Dimensions of various filter elements used in this work are listed in Table II. Due to the limited computational resources, it was not possible to arbitrarily extend the input and output regions. If the input and output regions are too short, the flow rate will be affected, as the boundary conditions described in Section II are suitable only for developed flows. To check whether the output section length is adequate, a commercial finite-element Navier–Stokes solver (ANSYS 5.3), with no-slip boundary conditions, was used to simulate filter 1, whose dimensions are given in Table II. The simulation was repeated with the output section length (l_{out}) increased to 20 μm. The results exhibited only a 1% change as compared to the original geometry. This implies that the length of the output domain used in our DSMC simulations is adequate. Except for the fact that there was no slip with the ANSYS 5.3 simulator, the qualitative behavior of the Navier–Stokes and the DSMC solutions showed agreement.

A. Flow Characteristics in Varying Filter Dimensions

1) Effect of Channel Length: The dependence of the flow characteristics on the channel length was investigated using filters 1, 2, and 4, which have the same channel height of 1 μm and channel lengths of 1, 5, and 10 μm, respectively (see Table II). The results of this study are shown in Figs. 7–11 along various cross-sections. To facilitate comparison, the x- and y-axes are shifted so that the center point of the channel is at $x = y = 0$.

Filters 1 and 3 were simulated on 195-MHz nodes using 64 and 11 CPUs, and filter 5 was simulated on 250-MHz nodes using 16 CPUs. The run times for filters 1, 3, and 5 were 26.7, 37.9, and 25.1 h, respectively. The run times of other simulations were in the same range. If these simulations were done on serial computers, the run times would have been approximately 1700, 420, and 400 h for filters 1, 3, and 5, respectively. Thus, parallel computers are inevitable to enable investigation of the flow features in microfilters using the DSMC technique.

Filter 1 has the smallest l_c/h_c ratio of the filters studied; thus the presence of undeveloped flow can be easily observed. For this filter, the pressure drop is nonlinear and extends beyond the membrane channel. The pressure drop in filters 1, 2, and 4 is shown in Fig. 7, and a closeup of the pressure drop in filter 1 is shown separately in Fig. 8. The nonlinear pressure drop in filter 1 is attributed to the undeveloped nature of the flow within the channel. The presence of undeveloped flow in filter 1 can also be observed in the velocity curve in Fig. 9. The flow in filters 2 and 4 is developed for a large section of the channel. This results in a linear pressure drop and a smoothly increasing velocity profile. The nonlinear pressure drop that is expected in compressible channel flows is not observed due to the small input-to-output pressure ratio. As a result, it can be concluded that for these filters, the pressure drop is very close to linear, unless the length-to-height ratio introduces effects due to undeveloped flow.

Velocity slip is observed for all the filters studied. The slip velocity on the channel walls is shown in Fig. 10. At the entrance and exit of the channel, undeveloped flow causes rapid change in slip velocity. Beyond these regions, slip velocity increases as expected from fully developed channel flow of gases [10]. Slip is also observed on membrane walls at the entrance and exit (see Fig. 11). The presence of slip on the membrane walls is due to the high local Kn close to the channel entrance. For filter 1, the local Kn at point p7 in Fig. 6, based on the variation of the y component of velocity, is 0.11.

The accommodating diffusive surfaces G and J act as a constant temperature heat bath that can supply energy to the expanding gas. The amount of energy transferred depends on the input pressure, pressure ratio, and degree of irreversibility. For filter 1, the energy transferred to and from the membrane surfaces G and J was estimated by summing the energies of all particles that hit these surfaces before and after the reflection. The result shows a net energy transfer of 31 W/cm^2 to the gas. For a real membrane with finite heat capacity, this energy transfer will result in cooling of the membrane. To prevent freezing of water vapor on the filter, this energy will need to be supplied by heating either the incoming flow or the filter membrane, unless the input gas is completely free of water vapor.

As shown in Fig. 12, for filter 1, a temperature drop of about 10 K is observed in the channel. This temperature drop can be attributed to the thermal energy being converted to the kinetic energy of the flow [7]. The resulting temperature change invalidates the isothermal flow assumption used in some analytical approaches for long channel problems. However, for filter 2 the temperature drop is not as strong and for filter 4 no temperature drop was observed. So isothermal flow assumption may still be applicable for filters 2 and 4. The temperature in the channel was constant at 300 K for the other filters listed in Table II.

2) Effect of Knudsen Number: The effect of Kn was investigated by studying filters 1, 3, and 5. The channel length l_c was kept constant at 1 μm and the channel height was set to values of 1, 0.2, and 0.05 μm, resulting in Kn of 0.054, 0.27, and 1.1, re-

TABLE II
DIMENSIONS OF VARIOUS FILTERS STUDIED AND FLOW RATES AT $\Delta P = 0.3$ atm

	Filter-1	Filter-2	Filter-3	Filter-4	Filter-5	Filter-6
$h_c(\mu m)$	1	1	0.2	1	0.05	0.2
$l_c(\mu m)$	1	5	1	10	1	2
$h_p(\mu m)$	5	5	1	5	1	1
$l_{in}(\mu m)$	4	6	4	4	4	4
$l_{out}(\mu m)$	7	7	5	7	7	5
Kn_{out}	0.054	0.054	0.27	0.054	1.1	0.27
Flow rate from DSMC $(m^3/(s-m^2))$	16.2	6.10	2.59	3.26	0.682	1.46
Channel flow rate from formula 1 $(m^3/(s-m^2))$	32.9	6.58	2.47	3.29	0.432	1.24
Reynolds number estimate	5.7	2.1	0.18	1.1	0.048	0.10

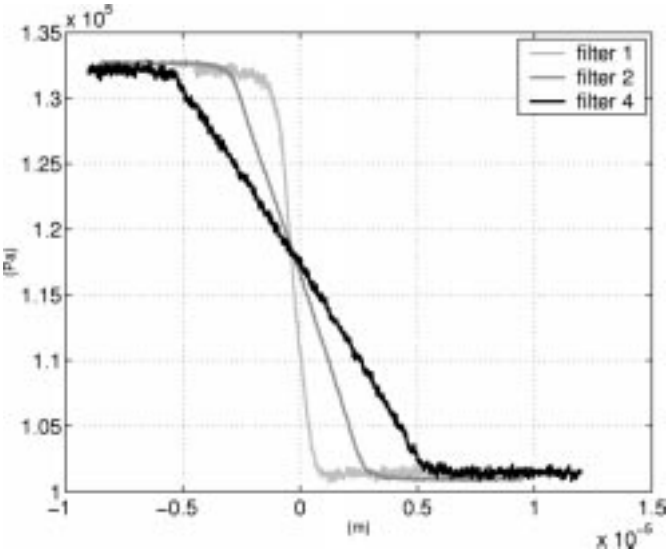

Fig. 7. Pressure along midline of the channel (line p1–p2 of Fig. 6).

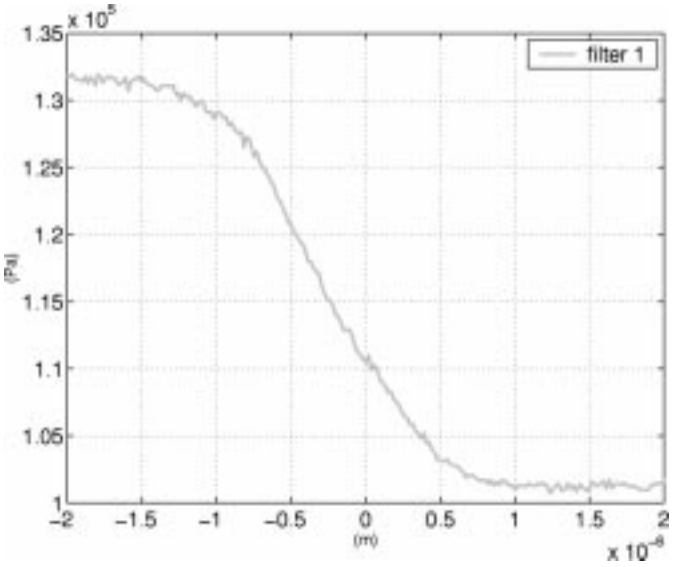

Fig. 8. Pressure along midline of the channel for filter 1 (line p1–p2 of Fig. 6).

spectively. Results for filters 1, 3, and 5 are compared in Figs. 13 and 14 along various cross-sections (x- and y-axes are shifted as before). The velocity along the midline drops sharply as channel height is decreased. However, due to larger rarefaction, the slip velocity does not drop as strongly. The result is a flatter flow profile as shown in Fig. 14. Thus, for higher values of Kn, the contribution of slip velocity to the flow rate is higher.

3) Flow Rates: From a system designer's point of view, the flow rate obtained from a filter is one of the most important characteristics. It is necessary to know when and to what extent simple analytical formulas will be adequate, when the Navier–Stokes solvers are valid, or when DSMC simulators are required. In this paper, DSMC results are compared with the analytical results for rarefied long channel flows, in order to gain insight. For a long channel, for which the length over height ratio is much greater than one, the volumetric flow rate at the input for an array of channels is given by [8]

$$\dot{v} = \frac{h_c^3 w P_o^2}{24 \mu l_c} \frac{\mathcal{P}^2 - 1 + 12\sigma Kn(\mathcal{P}-1)}{P_{\text{in}}} \tag{1}$$

where

P_o output pressure;
μ viscosity;
l_c channel length;
P_{in} input pressure;
σ momentum accommodation coefficient, and $\mathcal{P} = \mathcal{P}_{\text{in}}/\mathcal{P}_{\text{out}}$.

This formula was derived using a first-order slip boundary condition [8]. Flow rates obtained from the DSMC simulations and the estimates obtained using the above analytical formula are listed in Table II.

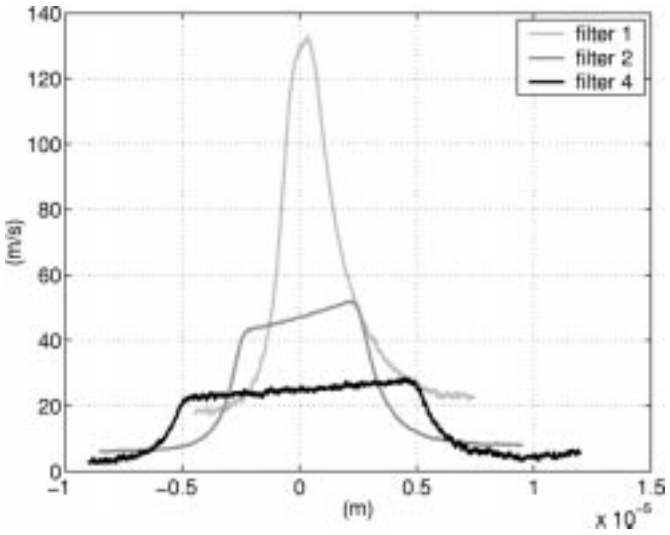

Fig. 9. X-velocity along midline of the channel (line p1–p2 of Fig. 6).

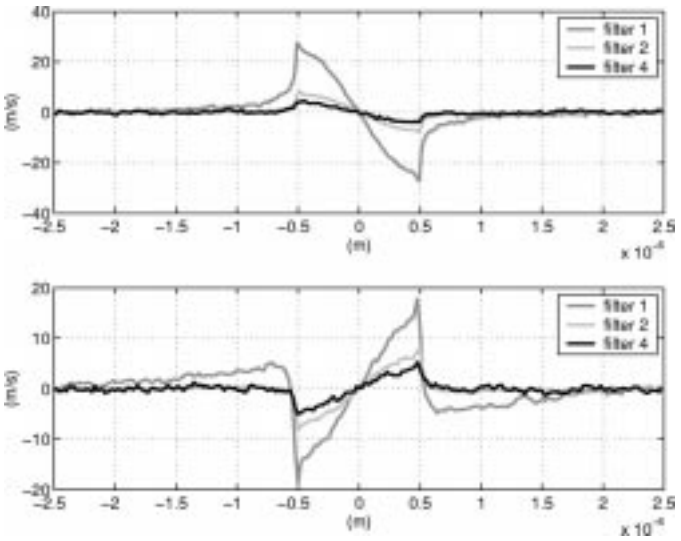

Fig. 11. Y-velocity along the input and exit walls (lines p4–p9 and p5–p10 of Fig. 6).

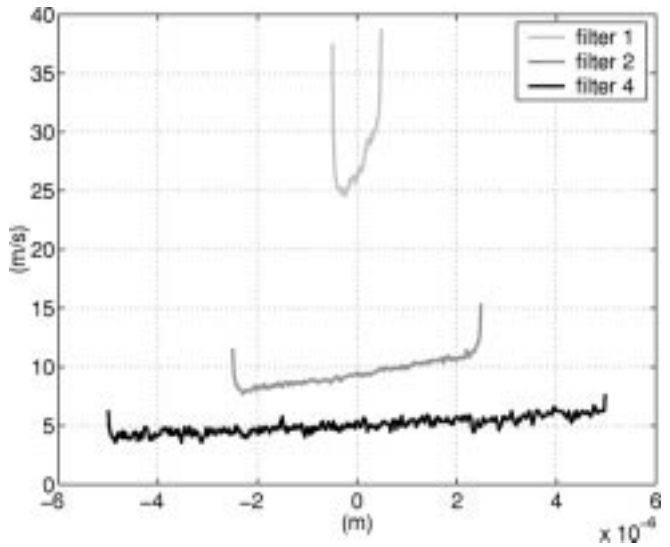

Fig. 10. X-velocity on the channel walls (line p7–p8 of Fig. 6).

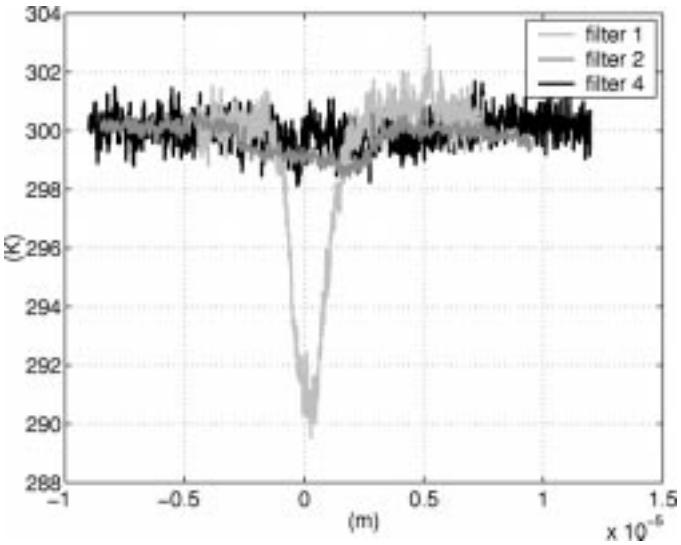

Fig. 12. Temperature along midline of the channel (line p1–p2 of Fig. 6).

For filters 1, 2, and 4, the simulated flow rates are smaller than the analytical estimates by 50.8%, 7.3%, and 0.9%, respectively. The observation that for filters 1, 2, and 4 the analytical estimates are larger than the DSMC solutions indicates that the entrance effects are dominant, and thus result in a decreased flow rate. For filter elements 3, 5, and 6, flow rates obtained by DSMC are larger than those calculated using the analytical formula by 4.8%, 57.9%, and 17.7%, respectively. This difference can be attributed to rarefaction effects. The slip velocity and rarefaction effects are underestimated by the 2-D analytical model. For $Kn > 0.10$, a disagreement between continuum and DSMC results is expected [8]. These results support the result that for $Kn < 0.10$, the analytical approach is adequate for membranes with long channels, and in other cases Navier–Stokes solvers with slip boundary conditions will be adequate. For $Kn > 0.10$, DSMC simulation is required to capture the rarefaction effects.

B. Dependence of Flow Rate on Pressure Difference

The dependence of the flow rate on the pressure difference is an important characteristic for microfilter elements. This behavior will affect the design of filter membranes. Especially early in the design cycle, this knowledge will be important to enable selection of an operational pressure difference range and a range of filter thicknesses.

It is necessary to evaluate the pressure-difference flow-rate characteristics in the presence of effects due to undeveloped flow and rarefaction. For this purpose, a test of dependence of the flow rate on the pressure difference was made by simulating filters 1 and 3 at different pressures. The output was kept at 1 atm and the input pressure was varied as shown in Fig. 15. In the same plot, the estimates from (1) are also shown.

For the pressure range studied, the dependence of flow rate on the pressure difference obtained by DSMC and by a 2-D channel approximation [(1)] are similar. For filter element 3, the

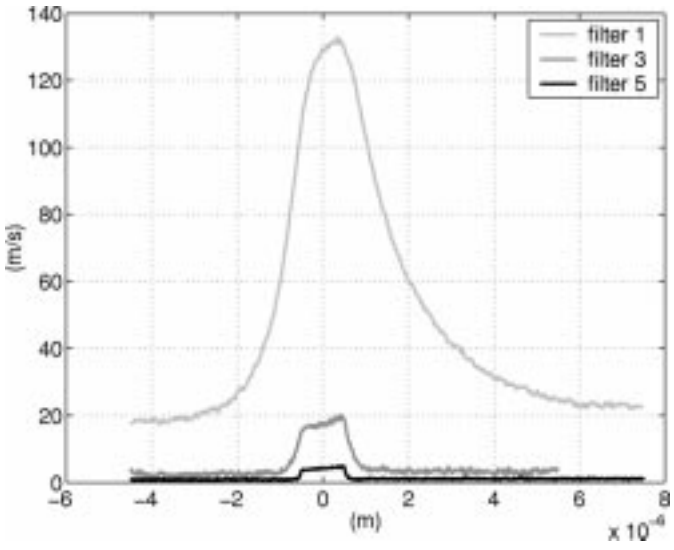

Fig. 13. X-velocity along midline of the channel (line p1–p2 of Fig. 6).

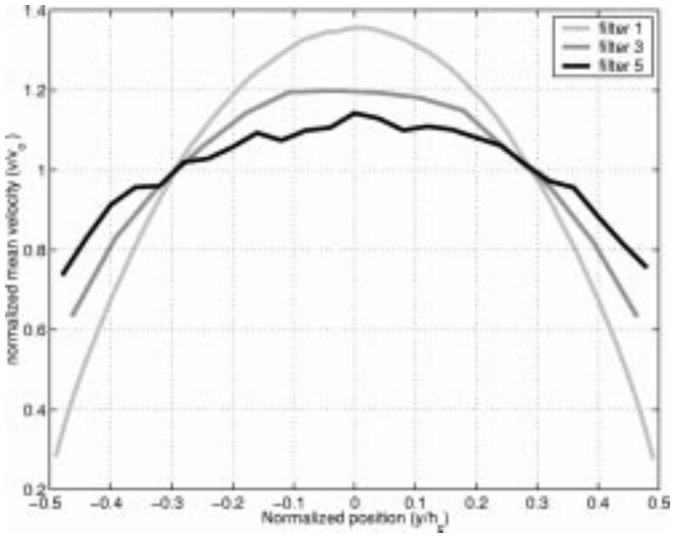

Fig. 14. X-velocity across the channel. v is the x-velocity averaged around line p11–p12 of Fig. 6 and v_o is the mean velocity in the same region.

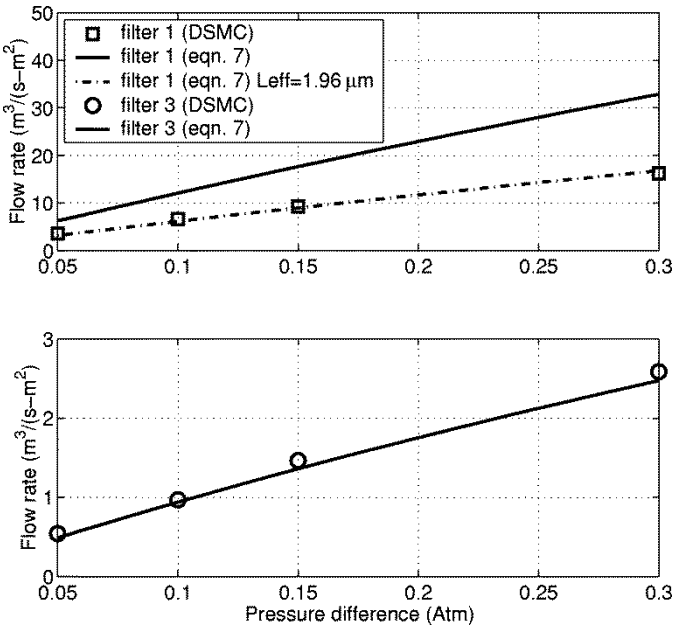

Fig. 15. Dependence of flow rate on the pressure difference for filters 1 and 3.

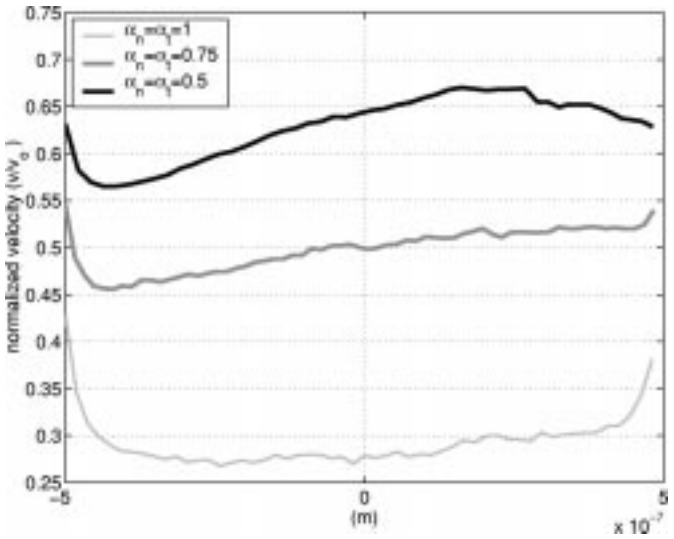

Fig. 16. X-velocity on the channel walls (line p7–p8 of Fig. 6). v is the x-velocity and v_o is the local mean velocity.

agreement between DSMC and 2-D channel results is again observed. For filter 1, even though there is a large disagreement on the value of the flow rate, there is an agreement on the general behavior. By using an effective length that is larger than the actual length, the result from (1) is shown to match the DSMC results for filter 1 (see Fig. 15). The effective length used was $l_c = 1.96\ \mu$m, as compared to the real length of $l_c = 1\ \mu$m. The design implication is that the gain in flow rate obtained by reducing the filter length decreases as the length is reduced. Furthermore, since the behavior exhibited in Fig. 15 is very close to linear, the optimal operational pressure of the filter will simply be the burst pressure with some margin for safety.

C. The Role of Accommodation Coefficient in Microfluidics

Incomplete accommodation is observed on very clean and smooth surfaces, or for cases where the surface atoms are much heavier than the gas molecules [8], [12]. In MEMS applications, microfabrication techniques can provide methods to engineer the surface material for achieving lower accommodation coefficients. To predict the effects of incomplete accommodation, flow characteristics in microfilters were simulated using the Cercignani–Lampis model [16] for surface scattering. For the simulations, tangential and normal energy accommodation coefficients were taken to be equal, that is, $\alpha_t = \alpha_n = \alpha$ was assumed. All physical surfaces (surfaces G and J in Fig. 6) were assumed to have the same value of accommodation coefficients. Filter 1 and filter 3 were simulated using $\alpha = 0.75$ and $\alpha = 0.5$. The results for filter 1 are shown in Figs. 16–20.

The reduction in the accommodation coefficients results in various changes in the flow. We observe that from Figs. 16 and 17, incomplete accommodation increases the slip velocities both at the channel walls and on the filter membrane. The ratio of the slip velocity for $\alpha = 0.75$ and $\alpha = 0.5$ to the slip velocity for fully accommodating surfaces $(\alpha = 1)$ is 2.5 and 3.5, respec-

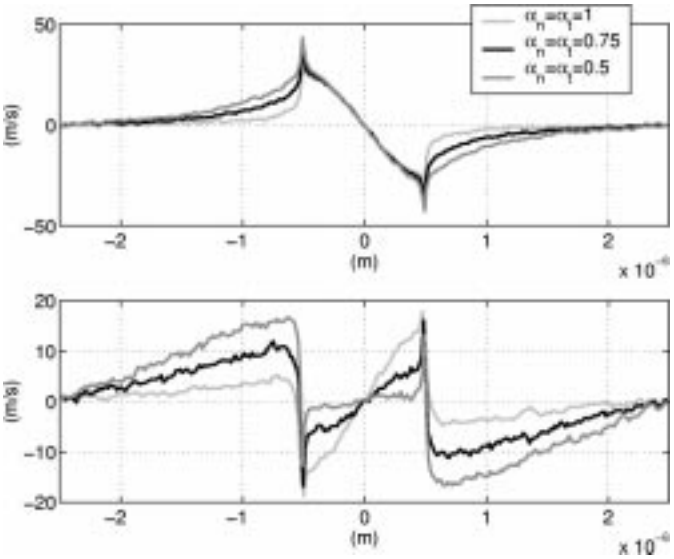

Fig. 17. Y-velocity on the input and exit walls (lines p4–p9 and p5–p10 of Fig. 6).

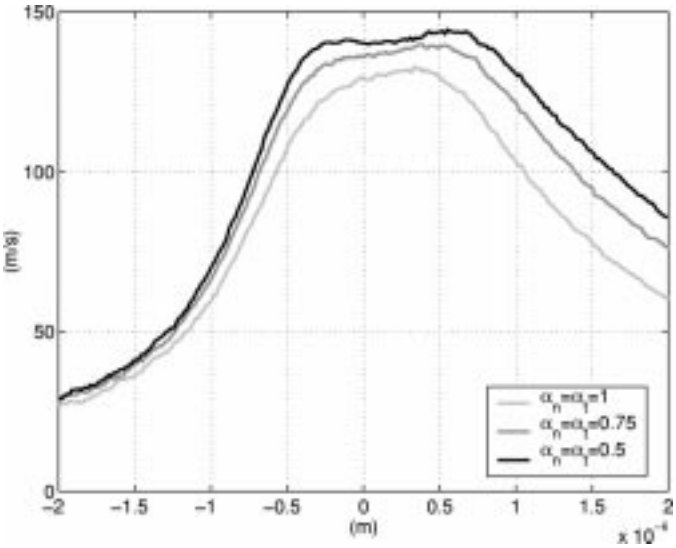

Fig. 18. Velocity along midline of the channel (line p1–p2 of Fig. 6).

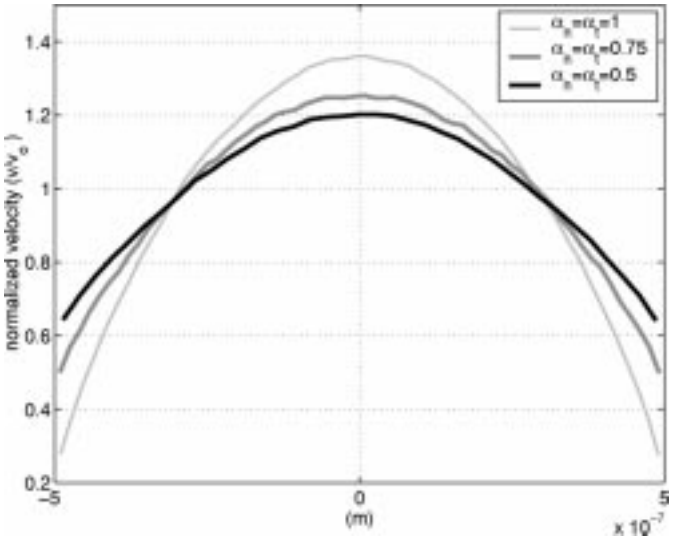

Fig. 19. X-velocity across the channel (line p11–p12 of Fig. 6). v is the x-velocity and v_o is the local mean velocity.

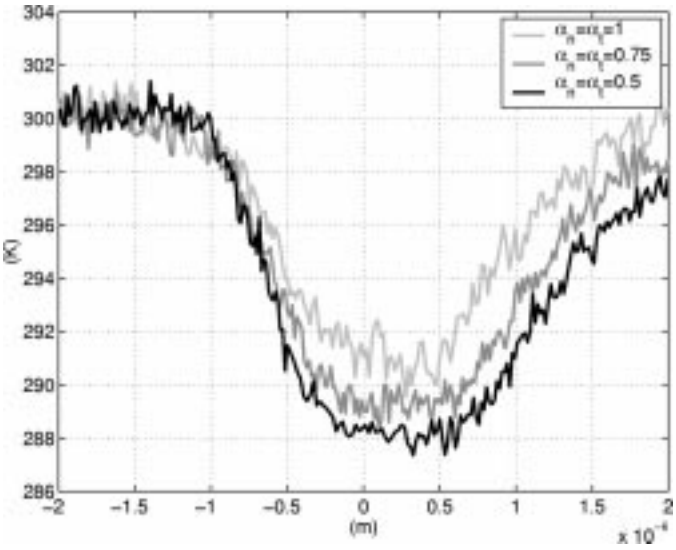

Fig. 20. Temperature along midline of the channel (line p1–p2 of Fig. 6).

tively. However, the velocity along the midline of the channel and the velocity across the channel do not increase by the same ratios, as shown in Figs. 18 and 19, respectively. The temperature profiles in Fig. 20 indicate the presence of a larger temperature drop for $\alpha < 1$, which can be attributed to the faster flow velocity, and weaker interaction with channel walls.

The flow rates obtained for filters 1 and 3 are listed in Table III. For filter 1, the flow rate for $\alpha = 0.75$ and $\alpha = 0.5$ is 11% and 20% larger, respectively, than the flow rate for $\alpha = 1.0$. For filter 3, the corresponding increase in flow rates is 65% and 120%, respectively. These results indicate that for a given value of α, the flow rate of filter 3 increases by a much larger percentage compared to the increase in flow rate of filter 1. The weak dependence of flow rate on accommodation coefficients for filter 1 can be explained by the small length-to-height ratio of its channel, which results in losses due to entrance flow. However, for filter 3, since the length-to-height ratio is larger, the flow rate is limited by the interaction of the gas with the walls, and an increase in slip velocity increases the flow rate. The large increase in the flow rate for low values of incomplete accommodation can be used to design more efficient filters.

TABLE III
DEPENDENCE OF FLOW RATES ON ACCOMMODATION COEFFICIENTS. THE FLOW RATES HAVE UNITS $(m^3/s - m^2)$. THE ACCOMMODATION COEFFICIENTS USED IN THE SIMULATIONS ARE $\alpha_n = \alpha_t = \alpha$

	$\alpha = 1.0$	$\alpha = 0.75$	$\alpha = 0.5$
Filter 1	16.2	18.0	19.5
Filter 3	2.59	4.35	5.74

D. Filter Element Proximity

The lithography-based fabrication techniques for microfilters generally produce an array of filter elements. For this reason, the filter geometry described in Fig. 6 uses periodic boundary conditions along lines C, E, D, and F to model an array of filter elements.

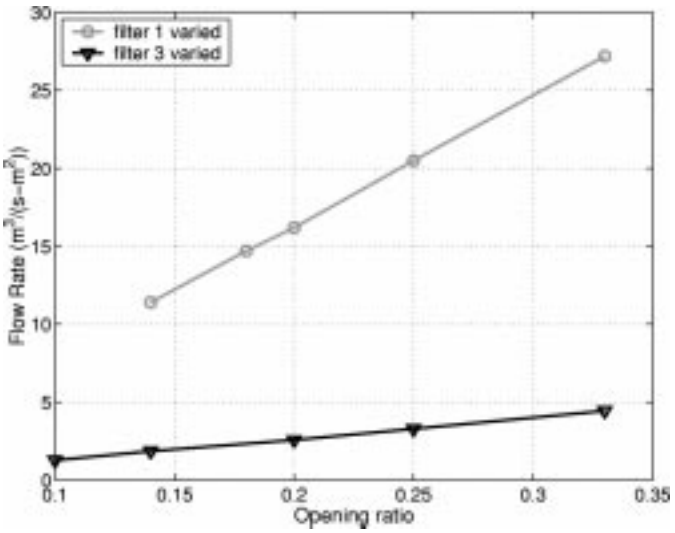

Fig. 21. Variation of flow rate with filter element period.

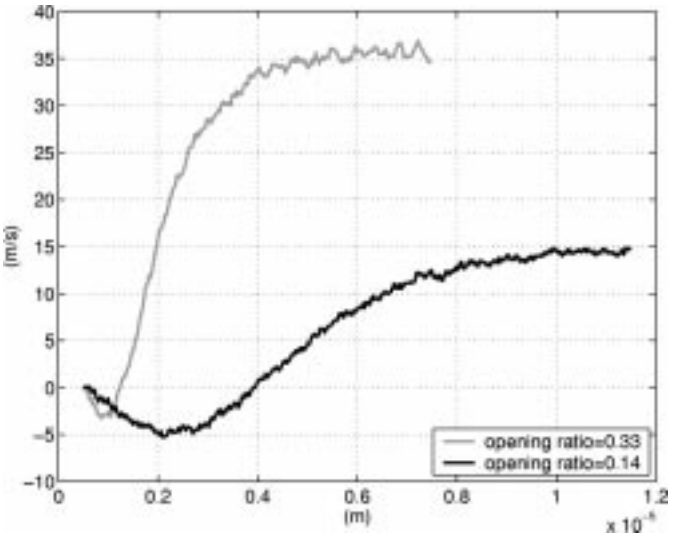

Fig. 22. Average x-velocity on lines E and F of Fig. 6.

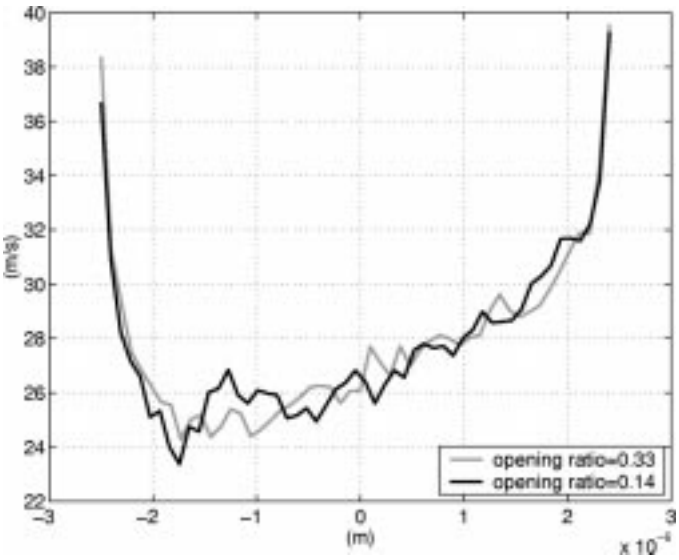

Fig. 23. X-velocity on channel surfaces for two different periodic lengths.

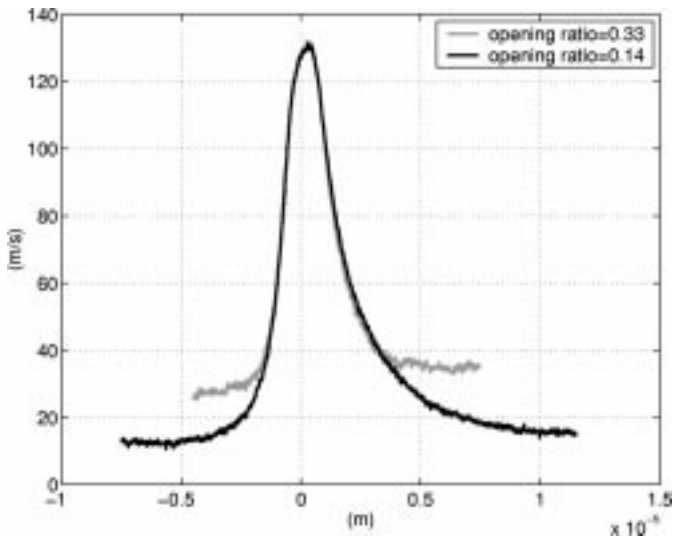

Fig. 24. X-velocity along midline of the channel for two different periodic lengths.

The effect of periodicity on the flow rate and on the flow characteristics in general was investigated by varying the period of filter elements 1 and 3. This was achieved by changing h_p in Fig. 6. The resulting flow rates are shown in Fig. 21 as a function of the opening ratio (h_c/h_p for this case). The flow rate shows a linear dependence on the opening ratio. This signifies that the interaction between neighboring filter elements is not strong enough to alter the flow characteristics within the channel. The effect of a change in h_p was investigated further by simulating filter 1 for $h_p = 3$ μm and $h_p = 7$ μm, corresponding to opening ratios of 0.33 and 0.14. For $h_p = 7$ μm, $l_{\text{in}} = 7$ μm and $l_{\text{out}} = 11$ μm were used. Fig. 22 shows that the length of the circulation region at the output decreases significantly with increasing opening ratio, i.e., as the filter elements get closer. However, the flow field in the channel does not change. The slip velocity on the channel surfaces, shown in Fig. 23, is almost independent of the change in the opening ratio. Similarly, the velocity in the channel does not change with the opening ratio, as shown in Fig. 24. As expected, in the input and output regions, the velocity is higher for higher opening ratio.

The above results suggest that for the range of filter sizes and pressure differences considered in this paper, the proximity of the filters does not influence the flow rate. This implies that for design purposes, two filter elements can be positioned as close as possible, without a tradeoff in the flow rate. For modeling purposes, the flow rate can be estimated accurately by simulating a single element and scaling the flow rate for the opening ratio.

VI. Conclusion

Microfilters were investigated in a configuration and operation regime that is of relevance for practical applications. The simulations in this paper show that DSMC can be used effectively to predict gas flows in microfluidic devices, as long as information on surface accommodation coefficients is available. Our results on 2-D microfilter geometries indicate the presence of velocity slip and increased flow rate. Slip velocity increases strongly for lower values of accommodation coefficients and

results in significant flow-rate increase for long channels. An effective channel length can be used with a 2-D long channel approximation formula to match the DSMC flow rate. Once an effective channel length is calculated for a filter for a given pressure difference, it is possible to estimate the flow rate for other pressure differences. The presence of several filter elements in a membrane does not alter the flow in a given channel. This observation enables the use of a single filter channel with periodic boundary conditions to estimate the behavior of a membrane with many filter channels. The heat transfer from the filter membrane to the gas is significant and needs to be investigated further with coupled simulations.

ACKNOWLEDGMENT

The authors would like to extend their thanks to the NCSA NT-SuperCluster group for the computer time on the initial phases of this research.

REFERENCES

[1] G. T. A. Kovacs, *Micromachined Transducers Sourcebook*. New York: McGraw-Hill, 1998.
[2] Y.-C. Tai, L.-S. Fan, and R. S. Muller, "IC-processed micro-motors: Design, technology and testing," in *Proc. IEEE Workshop Micro Electro Mechanical Systems*, Salt Lake City, UT, Feb. 20–22, 1989, pp. 1–6.
[3] W. C. Tang, H. Nguyen, M. W. Judy, and R. T. Howe, "Electrostatic-comb drive of lateral polysilicon resonators," *Sens. Actuators*, vol. A21, no. 1–3, pp. 328–331, Feb. 1990.
[4] X. Yang, J. M. Yang, X. Q. Wang, E. Meng, Y. C. Tai, and C. M. Ho, "Micromachined membrane particle filters," in *Proc. 11th Annu. Int. Workshop Micro Electro Mechanical Systems (MEMS'98)*, Germany, Jan. 25–29, 1998, pp. 137–142.
[5] W.-H. Chu, R. Chin, and M. Ferrari, "Silicon membrane nanofilters from sacrificial oxide removal," *J. Microelectromech. Syst.*, vol. 8, no. 1, pp. 34–42, Mar. 1999.
[6] W.-L. Li, "Analytical modeling of ultra-thin gas squeeze film," *Nanotechnology*, vol. 10, pp. 440–446, 1999.
[7] A. Beskok and G. E. Karniadakis, "A model for flows in channels, pipes and ducts at micro and nano scales," *Microscale Thermophys. Eng.*, vol. 3, no. 1, pp. 43–77, 1999.
[8] E. B. Arkilic, M. A. Schmidt, and K. S. Breuer, "Gaseous slip flow in long microchannels," *J. Microelectromech. Syst.*, vol. 6, no. 2, pp. 167–178, Jun. 1997.
[9] D. Zalesnik, M. M. Micci, and L. N. Long, "Direct simulation Monte Carlo model of low Reynolds number nozzle flows," *J. Propulsion Power*, vol. 10, no. 4, pp. 546–553, July–Aug. 1994.
[10] E. S. Piekos and K. S. Breuer, "DSMC modeling of micromechanical devices," in *Proc. AIAA Thermophysics Conf. (AIAA 95-2089)*, 1995.
[11] F. J. Alexander, A. L. Garcia, and B. J. Alder, "Direct simulation Monte Carlo for thin-film bearings," *Phys. Fluids*, vol. 6, no. 12, pp. 3854–3860, Dec. 1994.
[12] G. A. Bird, *Molecular Gas Dynamics and the Direct Simulation of Gas Flows*. New York: Oxford Univ. Press, 1994.
[13] E. S. Oran, C. K. Oh, and B. Z. Cybyk, "Direct simulation Monte Carlo: Recent advances and application," *Annu. Rev. Fluid Mech.*, vol. 30, pp. 403–441, 1998.
[14] W. Wagner, "A convergence proof for Bird's direct simulation Monte Carlo method for the Boltzmann equation," *J. Stat. Phys.*, vol. 66, pp. 1011–1044, 1992.
[15] G. Chen and I. D. Boyd, "Statistical Error Analysis for the direct simulation Monte Carlo method,", AIAA Paper 95-2316.
[16] R. G. Lord, "Some extensions to the Cercignani-Lampis gas-surface scattering kernel," *Phys. Fluids*, vol. A3, no. 4, pp. 706–710, Apr. 1991.
[17] C. Cercignani and M. Lampis, "Kinetic models for gas-surface interactions," *Transport Theory Statist. Phys.*, vol. 1, no. 2, pp. 101–114, 1971.
[18] S. A. Schaff and P. L. Chambre, *Fundamentals of Gas Dynamics*. Princeton, NJ: Princeton Univ. Press, 1958.
[19] S. Dietrich and I. D. Boyd, "Scalar and parallel optimized implementation of the direct simulation Monte Carlo method," *J. Computat. Phys.*, vol. 126, pp. 328–342, 1996.
[20] G. J. LeBeau, "A parallel implementation of the direct simulation Monte Carlo method," *Comput. Methods Appl. Mech. Eng.*, vol. 174, pp. 319–337, 1999.
[21] M. A. Rieffel, "A method for estimating the computational requirements of DSMC simulations," *J. Computat. Phys.*, vol. 149, pp. 95–113, 1999.

Ozgur Aktas received the B.S. degree in electrical engineering from the Middle East Technical University, Ankara, Turkey, in 1993 and the M.S. degree from the University of Illinois at Urbana-Champaign in 1997, where he is currently pursuing the Ph.D. degree in electrical and computer engineering.

He is with the Computational Electronics group, Beckman Institute for Advanced Science and Technology, University of Illinois. His research interests are in the areas of micro- and nanoscale devices.

N. R. Aluru (M'00) received the B.S. degree (with honors and distinction) from the Birla Institute of Technology and Science, Pilani, India, in 1989, the M.S. degree from Rensselaer Polytechnic Institute, Troy, NY, in 1991, and the Ph.D. degree from Stanford University, Stanford, CA, in 1995.

He was a Postdoctoral Associate at the Massachusetts Institute of Technology, Cambridge, from 1995 to 1997. In 1998, he joined the Department of General Engineering, University of Illinois, Urbana-Champaign (UIUC), as an Assistant Professor. He is affiliated with the Beckman Institute for Advanced Science and Technology, the Department of Electrical and Computer Engineering, and the Department of Mechanical and Industrial Engineering at UIUC. His current research interests are in the areas of computational methods, MEMS, microfluidics, bio-MEMS, NEMS, and bionanotechnology.

Dr. Aluru received the 1999 National Science Foundation CAREER award.

Umberto Ravaioli (M'88–SM'93) received the Laurea Dr. degree in electronics engineering and in physics from the University of Bologna, Italy, in 1980 and 1982, respectively. He received the Ph.D. degree in electrical engineering from Arizona State University, Tempe, in 1986.

He joined the Department of Electrical and Computer Engineering, University of Illinois at Urbana-Champaign, in 1986, where he is now a Professor. His research interests are in the areas of Monte Carlo device simulation, nanoelectronics, quantum transport, MEMS simulation, and supercomputation.

Prof. Ravaioli is a Fellow of the Institute of Physics.